

## Two-fluid physics and field-reversed configurations<sup>a)</sup>

A. Hakim<sup>b)</sup>

*Tech-X Corporation, 5621 Arapahoe Avenue – Suite A, Boulder, Colorado 80303*

U. Shumlak

*Aerospace and Energetics Research Program, University of Washington, Seattle, Washington 98195-2600*

(Received 6 November 2006; accepted 30 April 2007; published online 24 May 2007)

In this paper, algorithms for the solution of two-fluid plasma equations are presented and applied to the study of field-reversed configurations (FRCs). The two-fluid model is more general than the often used magnetohydrodynamic (MHD) model. The model takes into account electron inertia, charge separation, and the full electromagnetic field equations, and it allows for separate electron and ion motion. The algorithm presented is the high-resolution wave propagation scheme. The wave propagation method is based on solutions to the Riemann problem at cell interfaces. Operator splitting is used to incorporate the Lorentz and electromagnetic source terms. The algorithms are benchmarked against the Geospace Environmental Modeling Reconnection Challenge problem. Equilibrium of FRC is studied. It is shown that starting from a MHD equilibrium produces a relaxed two-fluid equilibrium with strong flows at the FRC edges due to diamagnetic drift. The azimuthal electron flow causes lower-hybrid drift instabilities (LHDI), which can be captured if the ion gyroradius is well resolved. The LHDI is known to be a possible source of anomalous resistivity in many plasma configurations. LHDI simulations are performed in slab geometries and are compared to recent experimental results. © 2007 American Institute of Physics. [DOI: 10.1063/1.2742570]

### I. INTRODUCTION

The dynamical behavior of plasmas is strongly dependent on frequency. At the lowest frequency, the motion of the electrons and ions are locked together by electrostatic forces and the plasma behaves like an electrically conducting fluid. This is the regime of magnetohydrodynamics (MHD). At somewhat higher frequencies, the electrons and ions can move relative to each other, behaving like two separate, interpenetrating fluids. At still higher frequencies, the distribution function of the plasma species is driven by anisotropies in the velocity space. This regime is best described by the collisionless Boltzmann equation or Vlasov equation of kinetic theory. In this paper, numerical schemes are developed to simulate two-fluid plasma dynamics, i.e., physics in the intermediate frequency regime between MHD and full kinetic theory. Due to the disparate scales on which plasma dynamics occurs, a complete spectrum of mathematical models of plasmas can be derived. Among the most commonly used fluid models are the magnetohydrodynamics model<sup>1</sup> and the Hall MHD model. In MHD, the plasma is treated as a single electrically conducting fluid. Although in the Hall-MHD model a distinction is made between the bulk plasma velocity and electron velocity, electron inertia and displacement currents are ignored and electron and ion number densities are assumed to be the same (quasineutrality). A more general approach, used in this paper, is to treat the plasma as a mixture of multiple fluid species. In this five-moment ideal two-fluid model, each plasma species is described by a set of fluid equations with electromagnetic body forces. The electromagnetic fields are modeled using Maxwell equations of

electromagnetism. The two-fluid model retains both electron inertia effects and the displacement currents and also allows for ion and electron demagnetization. The rest of this paper is organized as follows. First, some aspects of ideal two-fluid physics are described. Length scales at which two-fluid effects become important are then derived. Next, a high-resolution wave-propagation scheme<sup>2</sup> for the solution of these equations is presented. This scheme, originally developed by LeVeque, has been extensively used to study fluid dynamics, elasticity, MHD,<sup>3</sup> etc. The algorithms are benchmarked against the Geospace Environmental Modeling (GEM) magnetic reconnection challenge problem. It is shown that the reconnection flux from the two-fluid model agrees well with that computed from full particle and hybrid simulations. Simulations of field-reversed configurations (FRCs) equilibria and lower-hybrid drift instability (LHDI) are presented.

### II. TWO-FLUID PHYSICS

The two-fluid plasma equations can be obtained by talking moments of the Boltzmann equation. Assuming no heat flow and a scalar fluid pressure, the following five-moment ideal two-fluid equations listed below are obtained for each species in the plasma:

$$\frac{\partial n}{\partial t} + \frac{\partial}{\partial x_j}(nu_j) = 0, \quad (1)$$

$$m \frac{\partial}{\partial t}(nu_k) + \frac{\partial}{\partial x_j}(p \delta_{kj} + mnu_k u_j) = nq(E_k + \epsilon_{kij} u_i B_j), \quad (2)$$

<sup>a)</sup>Paper G12 3, Bull. Am. Phys. Soc. 51, 100 (2006).

<sup>b)</sup>Invited speaker.

$$\frac{\partial \mathcal{E}}{\partial t} + \frac{\partial}{\partial x_j} (u_j p + u_j \mathcal{E}) = q n u_j E_j. \quad (3)$$

Here  $n$  is the number density,  $\mathbf{u}$  is the mean fluid velocity,  $p$  is the fluid scalar pressure, and  $\mathcal{E}$  is the fluid total energy given by

$$\mathcal{E} = \frac{p}{\gamma - 1} + \frac{1}{2} m n u_i u_i, \quad (4)$$

where  $\gamma=5/3$  is the adiabatic index. Further  $\mathbf{E}$  is the electric field,  $\mathbf{B}$  is the magnetic flux density,  $q$  and  $m$  are the charge and mass of the plasma species, and  $\epsilon_{kmj}$  is the completely antisymmetric Levi-Civita pseudotensor, which is defined to be  $\pm 1$  for even/odd permutations of (1,2,3) and zero otherwise. Summation over repeated indices is assumed. The electromagnetic fields appearing in the source terms of the fluid equations are determined using Maxwell equations,<sup>4</sup>

$$\nabla \times \mathbf{E} = - \frac{\partial \mathbf{B}}{\partial t}, \quad (5)$$

$$\nabla \times \mathbf{B} = \mu_0 \mathbf{J} + \frac{1}{c^2} \frac{\partial \mathbf{E}}{\partial t}, \quad (6)$$

$$\nabla \cdot \mathbf{E} = \frac{\rho_c}{\epsilon_0}, \quad (7)$$

$$\nabla \cdot \mathbf{B} = 0. \quad (8)$$

Here  $\mu_0$  and  $\epsilon_0$  are the permeability and permittivity of free space,  $c = (\mu_0 \epsilon_0)^{-1/2}$  is the speed of light, and  $\rho_c$  and  $\mathbf{J}$  are the charge density and the current density defined by

$$\rho_c \equiv \sum q n, \quad (9)$$

$$\mathbf{J} \equiv \sum q n \mathbf{u}. \quad (10)$$

The summations in Eqs. (9) and (10) are over all species present in the plasma. For a plasma with  $s$  species, there are  $5s+8$  equations in the system.

The ideal two-fluid model is more general than the MHD or the Hall-MHD models. To derive conditions under which two-fluid effects, not included in the MHD or Hall MHD model, are important, scalar and vector potentials,  $\phi$  and  $\mathbf{A}$ , are introduced. In terms of these, the electric and magnetic fields are expressed as

$$\mathbf{E} = - \nabla \phi + \partial \mathbf{A} / \partial t, \quad (11)$$

$$\mathbf{B} = \nabla \times \mathbf{A}. \quad (12)$$

Next, defining a generalized momentum,  $\mathbf{P} \equiv m \mathbf{u} + q \mathbf{A}$  and a generalized vorticity,  $\boldsymbol{\Omega} \equiv \nabla \times \mathbf{P} = m \boldsymbol{\omega} + q \mathbf{B}$ , where  $\boldsymbol{\omega} = \nabla \times \mathbf{u}$  is the fluid vorticity, the nonconservative form of the momentum equation is written as

$$\frac{\partial \mathbf{P}}{\partial t} - \mathbf{u} \times \boldsymbol{\Omega} = - \frac{\nabla p}{n} + \nabla (m u^2 / 2 + \phi), \quad (13)$$

which is a balance law for the generalized momentum.<sup>5</sup> Taking the curl of Eq. (13) gives

$$\frac{\partial \boldsymbol{\Omega}}{\partial t} - \nabla \times (\mathbf{u} \times \boldsymbol{\Omega}) = - \nabla \times (\nabla p / n). \quad (14)$$

This equation applies to each species in the plasma, and, for example for a hydrogen plasma, there are two such equations. Equation (14) can be compared to the ideal MHD result

$$\frac{\partial \mathbf{B}}{\partial t} - \nabla \times (\mathbf{v} \times \mathbf{B}) = 0, \quad (15)$$

where  $\mathbf{v}$  is the ‘‘bulk’’ or MHD single-fluid velocity, the Hall-MHD result<sup>6</sup>

$$\frac{\partial \mathbf{B}}{\partial t} - \nabla \times (\mathbf{u}_e \times \mathbf{B}) = - \nabla \times (\nabla p_e / e n), \quad (16)$$

where  $e$  is electron charge, and the Euler (neutral) fluid result

$$\frac{\partial \boldsymbol{\omega}}{\partial t} - \nabla \times (\mathbf{v} \times \boldsymbol{\omega}) = - \nabla \times (\nabla p / \rho), \quad (17)$$

where  $\rho$  is the mass density. From these equations, it is clear that the two-fluid equations span the complete range from neutral fluids, to Hall-MHD, to MHD:  $\mathbf{B} \rightarrow \mathbf{0}$  corresponds to the neutral fluid limit,  $m_e / m_i \rightarrow 0$  corresponds to Hall-MHD, while  $\omega / (qB/m) \rightarrow 0$ , which, as shown below, is the same as vanishing electron and ion skin depths or ion Larmor radii, corresponds to the ideal MHD limit.

Examining the generalized vorticity  $\boldsymbol{\Omega} = m(\boldsymbol{\omega} + q\mathbf{B}/m)$  it is clear that for two-fluid effects to be important,

$$\omega / \omega_c \geq O(1), \quad (18)$$

where  $\omega_c \equiv qB/m$  is the cyclotron frequency. Using the fluid thermal velocity  $u_T \equiv \sqrt{2p/(mn)}$  as a reference speed and some reference length  $L$ ,  $\omega \approx u_T/L$  and hence the condition

$$u_T / (L \omega_c) = r_L / L \geq O(1), \quad (19)$$

where  $r_L \equiv u_T / \omega_c$  is defined as the Larmor radius, is obtained. Instead of the fluid thermal velocity, if the typical speed is assumed to be the Alfvén speed,  $u_A \equiv B / \sqrt{\mu_0 m n}$ , then the condition

$$u_A / (L \omega_c) = (c / \omega_p) / L \geq O(1), \quad (20)$$

where  $\omega_p \equiv \sqrt{n q^2 / \epsilon_0 m}$  is the plasma frequency, is obtained. It should be emphasized that the plasma frequency, Larmor radii, and cyclotron frequency are each defined separately for each plasma species.

In summary, two-fluid effects are important when, for both ions and electrons,  $r_L / L \geq O(1)$  and/or when  $l / L \geq O(1)$ , where  $l \equiv c / \omega_p$  is the skin depth. Conversely, in the limit in which the length scales are much larger than the electron skin depth, but smaller than the ion skin depth, Hall-MHD is an adequate model, while in the limit in which the scale lengths are larger than ion skin depths, the MHD description is adequate.

### III. HIGH-RESOLUTION WAVE PROPAGATION SCHEME

Inhomogeneous partial differential equations with hyperbolic homogeneous parts are called balance laws and arise in a large number of physical applications. Balance laws are put in the generic divergence form

$$\frac{\partial \mathbf{q}}{\partial t} + \nabla \cdot \mathbf{f} = \mathbf{s}, \quad (21)$$

where  $\mathbf{q}$  represents the conserved variables,  $\mathbf{f}$  the fluxes, and  $\mathbf{s}$  the source terms. For  $m$  balance laws in  $d$  spatial dimensions  $\mathbf{q}, \mathbf{s} \in \mathbb{R}^m$  and  $\mathbf{f} \in \mathbb{R}^{m \times d}$ . A conservation law is said to have a hyperbolic homogeneous part if for all unit vectors  $\boldsymbol{\omega} \in \mathbb{R}^d$  the flux Jacobian,  $\mathbf{A} \in \mathbb{R}^{m \times m}$ , defined by

$$\mathbf{A} \equiv \frac{\partial(\mathbf{f} \cdot \boldsymbol{\omega})}{\partial \mathbf{q}}, \quad (22)$$

has real eigenvalues and a complete set of right eigenvectors.<sup>2,7</sup> If, further, the eigenvalues are all distinct, the homogeneous part is called strictly hyperbolic. It can be shown that the five-moment ideal two-fluid equations have hyperbolic homogeneous parts. It can also be shown that higher-moment approximations to the Vlasov equations are also hyperbolic. Hence the high-resolution wave-propagation method, briefly described below, can be directly applied to such equations. For a complete description of this method, see LeVeque.<sup>2,8,9</sup>

In two dimensions, a homogeneous hyperbolic equation is written as

$$\frac{\partial \mathbf{q}}{\partial t} + \frac{\partial \mathbf{f}_1}{\partial x} + \frac{\partial \mathbf{f}_2}{\partial y} = 0, \quad (23)$$

where  $\mathbf{f}_1$  and  $\mathbf{f}_2$  are the fluxes in the  $X$  and  $Y$  direction, respectively. This equation is discretized on a rectangular domain  $\Omega \in [x_a, x_b] \times [y_a, y_b]$  by introducing cells  $I_{ij} = [x_{i-1/2}, x_{i+1/2}] \times [y_{j-1/2}, y_{j+1/2}]$ , where  $x_{i-1/2}$  and  $y_{j-1/2}$  are coordinates along cell edges and  $(x_i, y_j)$ , where  $x_i \equiv (x_{i-1/2} + x_{i+1/2})/2$  and  $y_j \equiv (y_{j-1/2} + y_{j+1/2})/2$ , are the coordinates of the cell center. Integrating the conservation law Eq. (23) over cell  $I_{ij}$  and from time  $t_n$  to  $t_{n+1}$ , the update formula

$$\begin{aligned} Q_{ij}^{n+1} &= Q_{ij}^n - \frac{\Delta t}{\Delta x} ([\mathcal{F}_1]_{i+1/2,j}^{n+1/2} - [\mathcal{F}_1]_{i-1/2,j}^{n+1/2}) \\ &\quad - \frac{\Delta t}{\Delta y} ([\mathcal{F}_2]_{i,j+1/2}^{n+1/2} - [\mathcal{F}_2]_{i,j-1/2}^{n+1/2}) \end{aligned} \quad (24)$$

is obtained. In this expression,  $Q_{ij}^n$  represents the cell average

$$Q_{ij}^n \approx \frac{1}{\Delta x \Delta y} \int_{y_{j-1/2}}^{y_{j+1/2}} \int_{x_{i-1/2}}^{x_{i+1/2}} \mathbf{q}(x, y, t) dx dy, \quad (25)$$

$\Delta x \equiv x_{i+1/2} - x_{i-1/2}$ ,  $\Delta y \equiv y_{j+1/2} - y_{j-1/2}$ ,  $\Delta t \equiv t_{n+1} - t_n$ , and  $[\mathcal{F}_{1,2}]$  are numerical fluxes at the cell interfaces defined as

$$[\mathcal{F}_1]_{i-1/2,j}^{n+1/2} \approx \frac{1}{\Delta t} \int_{t_n}^{t_{n+1}} \mathbf{f}_1(q(x_{i-1/2}, y_j, t), x_{i-1/2}, y_j) dt, \quad (26)$$

$$[\mathcal{F}_2]_{i,j-1/2}^{n+1/2} \approx \frac{1}{\Delta t} \int_{t_n}^{t_{n+1}} \mathbf{f}_2(q(x_i, y_{j-1/2}, t), x_i, y_{j-1/2}) dt. \quad (27)$$

Equation (24) is a general update formula for finite volume schemes, and several different methods can be constructed by selecting various approximations for the numerical fluxes. In this paper, a specific finite volume method, the high-resolution wave propagation method, introduced by LeVeque is used. To introduce this method, it should be first noted that at a given cell interface, the value of the cell averages in the cells sharing that edge will be, in general, discontinuous. This suggests that the numerical flux at the cell edge is determined by solving a Riemann problem at that edge.

The Riemann problem is an initial value problem,

$$\frac{\partial \mathbf{q}}{\partial t} + \frac{\partial \mathbf{f}_1}{\partial x} = 0, \quad x \in \mathbb{R} \quad (28)$$

with initial conditions  $\mathbf{q}(x < 0, 0) = \mathbf{q}_l$  and  $\mathbf{q}(x > 0, 0) = \mathbf{q}_r$ , where  $\mathbf{q}_{l,r}$  are constant vectors. For linear hyperbolic systems, the Riemann problem has exact solutions. For nonlinear problems, a linearization is introduced to obtain solutions valid around  $x=0$  for short time intervals. Assuming that Eq. (28) is a linear hyperbolic equation, it is written as

$$\frac{\partial \mathbf{q}}{\partial t} + \mathbf{A}_1 \frac{\partial \mathbf{q}}{\partial x} = 0, \quad (29)$$

where  $\mathbf{A}_1$  is the flux Jacobian and is constant for the assumed linear system. Let  $l^p$ ,  $r^p$ , and  $s^p$  be the left eigenvectors, right eigenvectors, and eigenvalues of  $\mathbf{A}_1$ . As the system is hyperbolic, the eigenvalues must be all real and the eigenvectors are assumed to be orthonormal. Multiplying by the left eigenvector  $l^p$ , a system of uncoupled wave equations

$$\frac{\partial w^p}{\partial t} + s^p \frac{\partial w^p}{\partial x} = 0 \quad (30)$$

is obtained, where  $w^p \equiv l^p \cdot \mathbf{q}$ . This has solutions  $w^p(x, t) = w_0^p(x - s^p t)$ , where  $w_0(x) = l^p \cdot \mathbf{q}(x, 0)$ . Once  $w^p(x, t)$  is determined,  $\mathbf{q}(x, t) = \sum_p w^p r^p$  and hence the Riemann problem for linear systems (or linearized systems) is solved exactly.

In the wave propagation method, the solution to the Riemann problem at each cell interface is used to derive the following approximation to the numerical fluxes:

$$\begin{aligned} [\mathcal{F}_1]_{i-1/2,j} &= \frac{1}{2} ([\mathbf{f}_1]_{i,j} + [\mathbf{f}_1]_{i-1,j}) \\ &\quad + \frac{1}{2} (\mathcal{A}_1^+ \Delta Q_{i-1/2,j} - \mathcal{A}_1^- \Delta Q_{i-1/2,j}). \end{aligned} \quad (31)$$

Introducing this expression in the update formula along with an analogous expression for the  $Y$  direction, numerical flux gives

$$\begin{aligned} Q_{ij}^{n+1} &= Q_{ij}^n - \frac{\Delta t}{\Delta x} [\mathcal{A}_1^+ \Delta Q_{i-1/2,j} + \mathcal{A}_1^- \Delta Q_{i+1/2,j}] \\ &\quad - \frac{\Delta t}{\Delta y} [\mathcal{A}_2^+ \Delta Q_{i,j-1/2} + \mathcal{A}_2^- \Delta Q_{i,j+1/2}]. \end{aligned} \quad (32)$$

In these expressions, the fluctuations  $\mathcal{A}_1^\pm \Delta Q_{i-1/2}$  (dropping the  $j$  subscript) stand for

$$\mathcal{A}_1^- \Delta Q_{i-1/2} = \sum_{p: s_{i-1/2}^p < 0} \mathcal{Z}_{i-1/2}^p + \frac{1}{2} Z_{i-1/2}, \quad (33)$$

$$\mathcal{A}_1^+ \Delta Q_{i-1/2} = \sum_{p: s_{i-1/2}^p > 0} \mathcal{Z}_{i-1/2}^p + \frac{1}{2} Z_{i-1/2}, \quad (34)$$

where

$$\mathcal{Z}_{i-1/2}^p = l_{i-1/2}^p \cdot ([\mathbf{f}_1]_i - [\mathbf{f}_1]_{i-1}) r_{i-1/2}^p, \quad (35)$$

and

$$Z_{i-1/2} = \sum_{p: s_{i-1/2}^p = 0} \mathcal{Z}_{i-1/2}^p. \quad (36)$$

In deriving Eq. (32), the identity

$$\mathcal{A}_1^- \Delta Q_{i-1/2} + \mathcal{A}_1^+ \Delta Q_{i-1/2} = \sum_p \mathcal{Z}_{i-1/2}^p = [\mathbf{f}_1]_i - [\mathbf{f}_1]_{i-1}, \quad (37)$$

which follows from the definition of  $\mathcal{Z}_{i-1/2}^p$  [see Eq. (35)], is used. The eigenvectors  $r_{i-1/2}^p$ ,  $l_{i-1/2}^p$ , and the eigenvalues  $s_{i-1/2}^p$  needed in these expressions are computed using the flux Jacobian at the cell interfaces. For linear system, this eigensystem is constant and does not depend on the solution. For nonlinear systems, an appropriate averaging must be used before determining the eigensystem. In the simulations presented here, Roe averages<sup>10</sup> are used for the Euler equations. Unlike conventional Godunov schemes, the wave propagation method presented above can also be applied directly to situations in which the fluxes explicitly depend on spatial coordinates. Further, it is not necessary that Roe averages be used (or even exist) for the hyperbolic system being solved: simple arithmetic averages are usually sufficient. It can be shown that even when Roe averages are not available, the scheme continues to be conservative.<sup>8</sup> Further, if Roe averages are used (or the system is linear) it can be shown that the zero wave,  $Z_{i-1/2}$ , vanishes.

Corrections can be added to make the scheme second-order accurate. These corrections can introduce unphysical oscillations near shocks, which can be removed by applying a limiter to the scheme. Further corrections, called transverse corrections, can also be added. With the transverse terms included in the update formula, the high-resolution wave propagation method is formally second order in space and time for general smooth two-dimensional flow problems. It should be mentioned that even if the transverse terms are not used, the scheme still gives second-order accuracy. However, with the transverse terms, the scheme is stable with Courant numbers of 1. Further, the solution with and without the transverse terms can be significantly different in some situations.

The source terms are handled using operator splitting. The homogeneous system is first solved separately and then the source terms are incorporated by solving the ordinary differential equation (ODE),

$$\frac{\partial \mathbf{q}}{\partial t} = \mathbf{s}. \quad (38)$$

To achieve second-order accuracy, and advance the complete solution by  $\Delta t$ , the ODE is first solved with time step  $\Delta t/2$ .

Then the homogeneous equation is solved with time step  $\Delta t$ . Finally, the ODE is again solved with time step  $\Delta t/2$ . Obviously, at each stage the results from the previous stage are used as initial conditions. This particular operator splitting scheme is known as Strang splitting. To solve the ODE Eq. (38), any standard ODE solution scheme (second order or higher) can be used. In this paper, a fourth-order Runge-Kutta scheme is used.

#### IV. COLLISIONLESS MAGNETIC RECONNECTION

Magnetic reconnection<sup>11</sup> is the process by which the topology of the magnetic field lines changes. In ideal MHD or ideal Hall-MHD, the field line topology cannot change and this is described by saying that field lines are ‘‘frozen’’ into the fluid (frozen into the electron fluid in the case of ideal Hall-MHD). The situation is analogous to neutral ideal fluid flow in which vortex tube topology remains constant. However, even small resistivity (viscosity in neutral fluids) can make the topology change and the field lines reconnect, and this process is adequately described in the framework of resistive MHD or Hall-MHD.

However, in a collisionless plasma, magnetic reconnection is also observed to occur and at a much faster rate than in collisional plasmas. This fast collisionless reconnection is important in understanding many space plasma phenomena, for example solar flares and the dynamics of the Earth’s magnetotail during a geomagnetic substorm. To understand the mechanism of collisionless reconnection, a number of plasma models were used to study collisionless reconnection of oppositely directed magnetic fields separated by a thin current sheet. This effort went under the rubric of Geospace Environmental Modeling (GEM) Reconnection Challenge.<sup>12</sup> The various models used were electron MHD,<sup>13</sup> Hall-MHD with anisotropic pressure,<sup>14</sup> MHD and Hall-MHD,<sup>15–17</sup> full particle,<sup>18</sup> and hybrid<sup>19</sup> models. It was found that although reconnection initiates at length scales on the order of the electron skin depth, the reconnection rate is governed by ion dynamics. The two-fluid model can describe the physics at electron skin depth scales and hence can describe collisionless reconnection correctly. On the electron-skin depth scales, the field lines are no longer frozen to the electron fluid and this allows the reconnection to initiate without the need for resistivity. On the other hand, in the Hall-MHD model,<sup>17</sup> the reconnection needs to be initiated by using a small resistivity.

To benchmark the algorithms, simulations are performed with the same initial conditions and parameters as used in the GEM Challenge problem. The ideal two-fluid model used here was not among one of those used in the original studies and hence serves as an important benchmark. The results obtained here also provide additional insight into the structure of the flow, especially after the reconnection has occurred. As is described below, complex flows, not observed in the results reported in the original studies, are obtained.

The simulation is initialized with oppositely directed magnetic fields separated by a thin current sheet. The magnetic field is given by

$$\mathbf{B}(y) = B_0 \tanh(y/\lambda) \mathbf{e}_x. \quad (39)$$

The initial current is carried only by the electrons,

$$\mathbf{J}_e = -\frac{B_0}{\lambda} \operatorname{sech}^2(y/\lambda). \quad (40)$$

The number densities of the ions and electrons are initialized as  $n_e(y) = n_i(y) = n(y)$ , where

$$n(y) = n_0 [1/5 + \operatorname{sech}^2(y/\lambda)]. \quad (41)$$

Finally, the electron pressure is set to  $p_e(y) = p(y)$  and ion pressure to  $p_i(y) = 5p(y)$ , where

$$p(y) = \frac{B_0}{12} n(y). \quad (42)$$

These initial conditions describe an equilibrium solution of the two-fluid equations. To initiate reconnection in a controlled manner, the magnetic field is perturbed with  $\delta \mathbf{B} = \mathbf{e}_z \times \nabla \psi$ , where

$$\psi(x, y) = \psi_0 \cos(2\pi x/L_x) \cos(\pi y/L_y), \quad (43)$$

and  $[-L_x/2, L_x/2] \times [-L_y/2, L_y/2]$  is the simulation domain. This form of the perturbation assures that  $\nabla \cdot \mathbf{B} = 0$  at  $t=0$ . Periodic boundaries are applied at  $x = \pm L_x/2$  and conducting wall boundaries at  $y = \pm L_y/2$ . Simulations presented below are for a  $512 \times 256$  grid, although coarser grids were also used. The other parameters used are  $m_e/m_i = 1/25$ ,  $L_x = 8\pi$ ,  $L_y = 4\pi$ ,  $B_0 = 0.1$ ,  $\psi_0 = B_0/10$ , and  $\lambda = 0.5$ . The unit length scale is the ion skin depth and the unit time scale is in inverse ion cyclotron frequency. For the selected electron-ion mass ratio, the electron skin depth is  $1/5$  and is resolved by the grid. These parameters are identical with the GEM challenge problem.

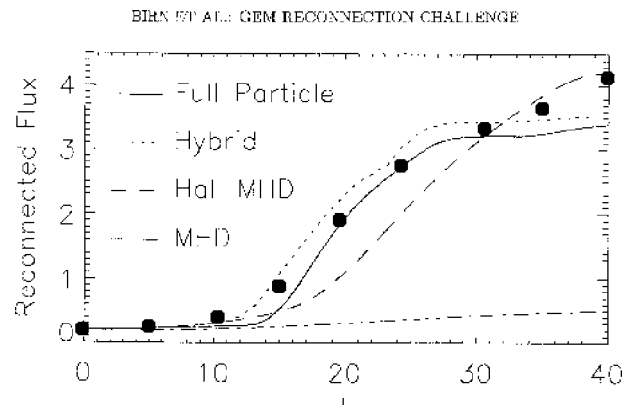


FIG. 1. Two-fluid reconnected flux compared to GEM results. Time in ion-cyclotron periods is plotted on the X axis and reconnected flux on the Y axis. Solid dots are results obtained using the two-fluid model. Two-fluid results compare well with those obtained by particle and hybrid models.

To compare results with the models used in the GEM challenge problem, the reconnected flux,  $\phi$ , was computed using

$$\phi(t) = \frac{1}{2L_x} \int_{-L_x/2}^{L_x/2} |B_y(x, y=0, t)| dx. \quad (44)$$

As the reconnection proceeds, the reconnected flux, which is a measure of the net  $Y$  direction magnetic field, increases and indicates the reconnection rate. Figure 1 shows the reconnected flux history. It is observed that the reconnection occurs at about  $t=10$  and the reconnected flux increases rapidly after that. The computed flux history is in excellent agreement with flux histories from full particle and hybrid models used in the original GEM Challenge problem. From the GEM results, it is also clear that the resistive Hall-MHD

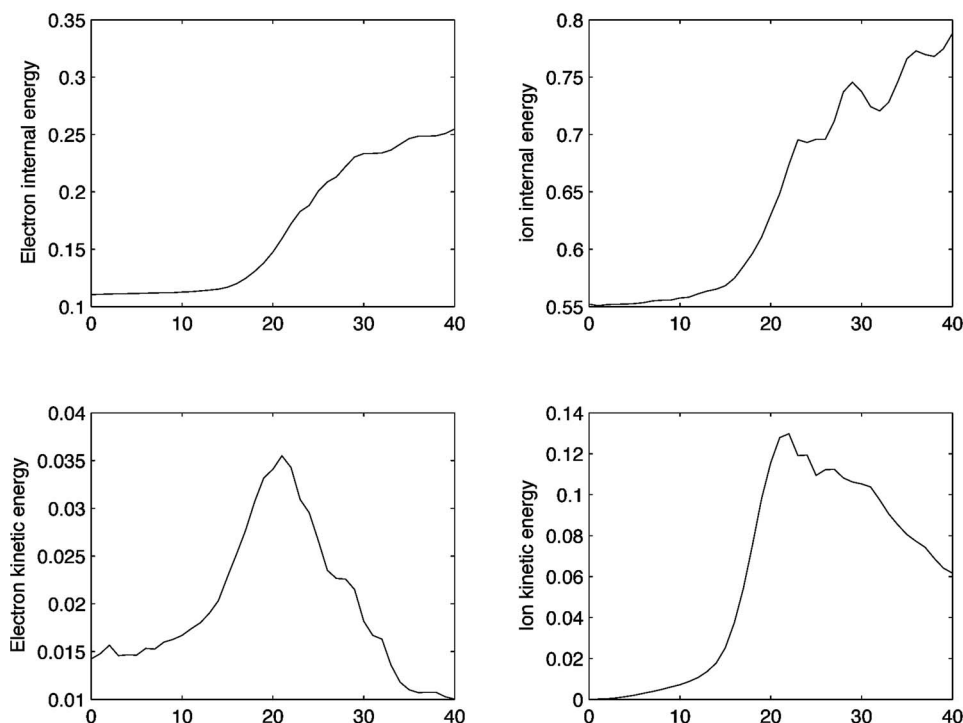


FIG. 2. Electron thermal energy (top left), ion thermal energy (top right), electron kinetic energy (bottom left), and ion kinetic energy (bottom right). Time in ion-cyclotron periods is plotted on the X axis. The electromagnetic kinetic energy released is transformed into kinetic and thermal energy of the fluids. After about  $t=25$ , fluid kinetic energies decay as fluids become turbulent.

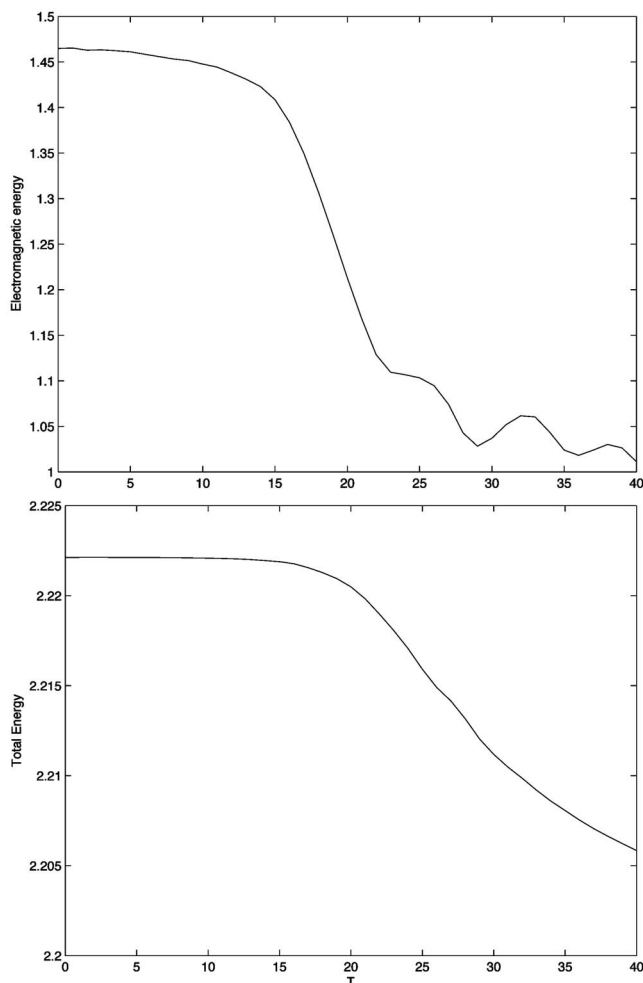


FIG. 3. Electromagnetic energy as a function of time (top) and total energy (bottom) for the GEM magnetic reconnection challenge problem. After reconnection occurs, the electromagnetic energy decays, the released energy being transformed to fluid thermal and kinetic energies. The total energy should remain conserved; however, it is seen to decay slightly due to numerical diffusion. The total loss in energy is 0.7% for the time period considered.

model also predicts the correct reconnected flux. However, in contrast to resistive Hall-MHD, the two-fluid model presented here does not have any resistivity. The reconnection initiates due to the demagnetization of the electrons at electron skin depth scales, and thus resistivity is not required to break the field lines as in Hall-MHD. Thus, in the two-fluid model the magnetic field-line topology is not tied to the electron fluid as it is in the ideal Hall-MHD.

As the domain is periodic in the  $Y$  direction and there are conducting walls on the  $x = \pm L_y/2$ , the total energy of the system remains constant in time. Figures 2 and 3 show the history of the electromagnetic and total energy of the system. The initial configuration of the system is an unstable equilibrium and via the process of reconnection the magnetic field “relaxes,” i.e., the electromagnetic energy stored in the magnetic field is transferred to the fluid energy. The electromagnetic energy decays rapidly after about  $t=10$  and is transferred to the fluid energy. After  $t=25$ , the fluid kinetic energy decreases and is transformed to the fluid thermal energy. Even though the fluids are inviscid, this conversion occurs

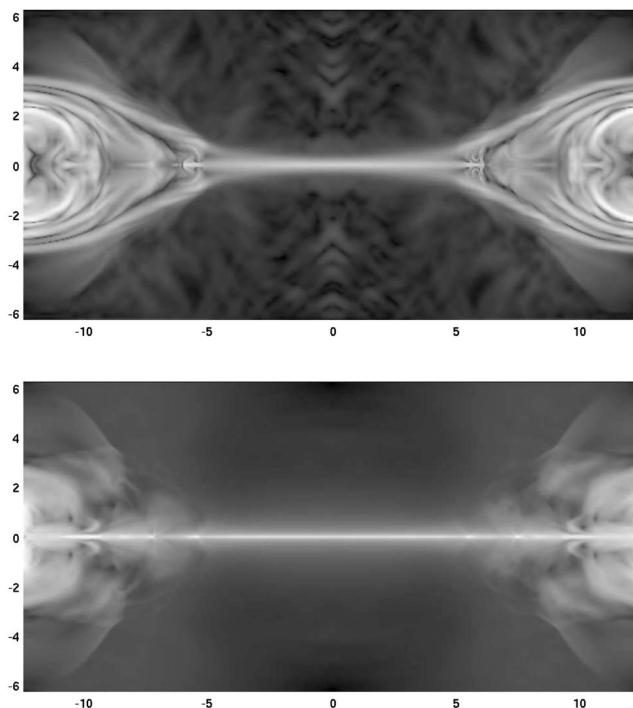


FIG. 4. Electron momentum (top) and ion momentum (bottom) at  $t=25$ . Inward traveling shock waves are visible in both fluids. Thin jets flowing along the  $X$  axis are also visible.

due to adiabatic compression of the fluid. Further, the fluid undergoes shock-heating as the shock waves, visible in Figs. 4 and 5, pass through the fluid.

Figure 3 shows the total energy of the system. The total energy should be conserved as the two-fluid system does not

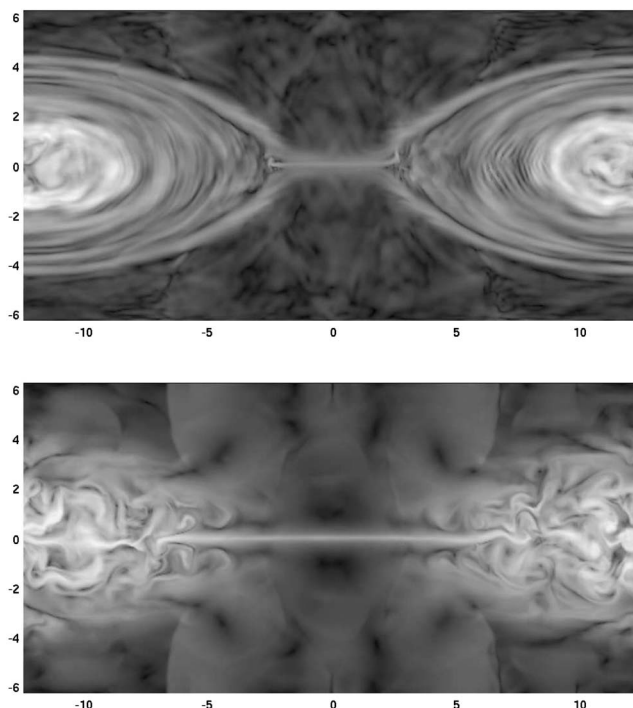


FIG. 5. Electron momentum (top) and ion momentum (bottom) at  $t=40$ . Complex flow features are visible, especially in the ion fluid. Flow structure is thought to develop due to instabilities.

have any dissipation, and conducting wall boundary conditions are used. However, due to numerical diffusion, the total energy reduces slightly. From the figure it is clear that the loss in energy is only about 0.7%, showing that the scheme used here is conservative even in the presence of complex flow features.

Electron and ion momentum at  $t=25$  and 40 are shown in the gray-scale plots, Figs. 4 and 5. At  $t=25$ , shock waves traveling inward (toward the  $Y$  axis) are observed. These shocks are formed due to the interaction of the outward flowing jets (along the  $X$  axis). At  $t=40$ , complex flow structures are seen in the ion fluid. The shocks at  $x \approx \pm 5.5$  are now moving outwards (away from the  $Y$  axis). The ion flow is not symmetric and this may be due to grid-driven instabilities. The nature of the flow at late times seems to be governed by instabilities driven from the counter-streaming fluid jets.

## V. AXISYMMETRIC TWO-FLUID EQUILIBRIA AND FIELD-REVERSED CONFIGURATIONS

The field-reversed configuration (FRC) and Spheromak<sup>20</sup> belong to the family of compact toroids. These devices do not have any internal material structures (“compact”), allowing the plasma to extend to the device axis. The magnetic field topology is that of a closed donut-shaped surface (“toroidal”). It is known that two-fluid effects play an important role in FRC physics. Two-fluid formalism to study FRC stability<sup>21–25</sup> has been developed extensively. Relaxation of two-fluid equilibria has also been studied.<sup>5</sup> However, no detailed numerical studies of FRCs using the two-fluid model have been performed before, although some results have been obtained using particle simulations.<sup>26</sup>

### A. Relaxation to two-fluid equilibrium

To study the nature of two-fluid equilibria, simulations were performed by initializing with an ideal MHD equilibrium. A rigid rotor solution for FRCs was selected. The FRC aspect ratio was assumed to be 5. Note that the initial conditions were computed using ideal-MHD and not two-fluid equilibrium, and hence the plasma undergoes a relaxation process into a new two-fluid equilibrium. In general, two-fluid equilibria are hard to compute, but the formalism has been developed for the full two-fluid equations by Steinhauer.<sup>5</sup>

The simulation was run until the plasma had relaxed to a new two-fluid equilibrium. The relaxed solutions are shown in Fig. 6. The density profiles show that the plasma has moved toward the FRC separatrix, possibly due to the centrifugal force of the rotating plasma. The velocity profiles of the electron and ion fluids are shown in Figs. 7. Diamagnetic drift due to the pressure gradients at the FRC edge causes strong azimuthal flow of the fluids.

### B. LHDI in cylindrical plasma configurations

Field-reversed configuration (FRC) is a plasma fusion device where the magnetic field is used to confine the plasma until fusion temperatures are reached and fusion initiates. In this section, FRC simulations are performed in the  $r$ - $\theta$  plane showing the formation of the lower-hybrid drift instability

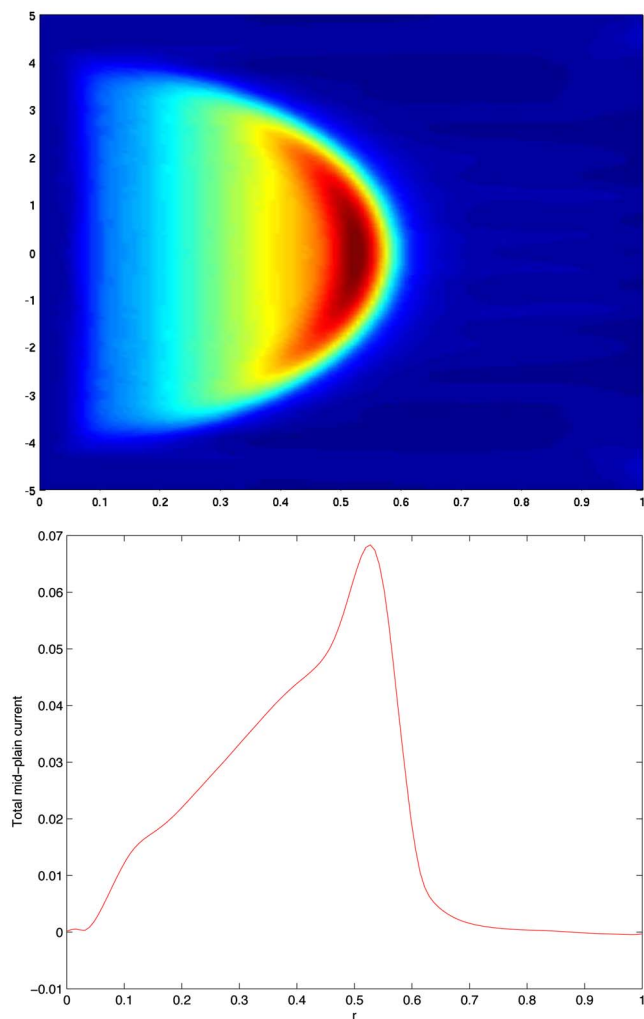


FIG. 6. Current density profile (top) and in the midplane (bottom) for a relaxed two-fluid equilibrium.

(LHDI) in FRCs. The two-fluid simulation performed in this section is for elongated FRCs in which  $\partial/\partial z \equiv 0$ . The initial conditions were computed from the two-fluid equilibrium equations obtained by setting  $\partial/\partial \theta \equiv 0$ ,  $u_r = 0$ , which, for stationary ions, are written as

$$-mn \frac{u_\theta^2}{r} = -\frac{\partial p}{\partial r} - enu_\theta B_z, \quad (45)$$

$$\frac{\partial B_z}{\partial r} = e\mu_0 mnu_\theta. \quad (46)$$

Here  $u_\theta$  is the electron azimuthal velocity,  $B_z$  is the magnetic field in the  $Z$  direction,  $p$  is the pressure, and  $-e$  is the electron charge. For an FRC, from the magnetic field  $B_z(r)$  changes sign across the domain. A number of “reversed field” magnetic profiles were selected. The electron current needed to support this field was computed from Eq. (46). Once  $u_\theta$  was determined, the pressure profile was determined from Eq. (45). Figure 8 shows the total electron momentum for one such magnetic field profile. The various simulations were performed by varying the magnetic field profile so as to control the thickness of the current sheet needed to support

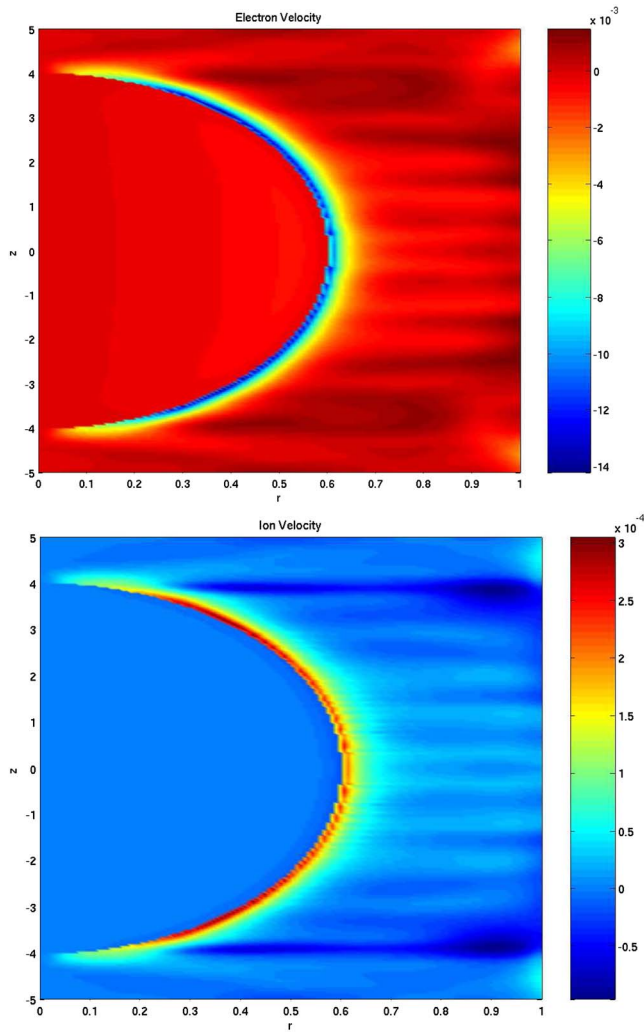


FIG. 7. Electron (top) and ion (bottom) and velocity on relaxations. The fluid shows strong azimuthal flow close to the outermost FRC flux surfaces.

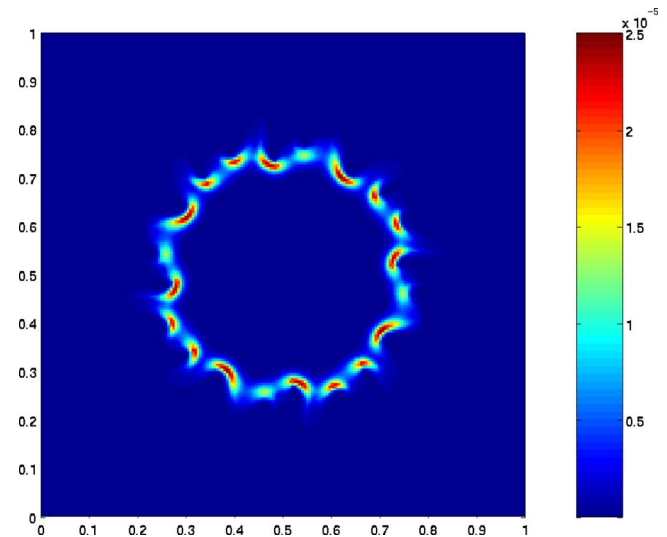


FIG. 9. Electron momentum in the  $r$ - $\theta$  plane for a field-reversed pinch at  $t=10$ . The current sheet has broken up into smaller structures, each of which is about an ion Larmor radius long.

the field. An initial  $m=1$  mode perturbation was applied to the electron momentum and the simulation was run to  $t=20$ . This initial perturbation corresponds to a long-wavelength (on the order of the current sheet length) perturbation. Time in these simulations was measured in light transit times across the domain.

Figure 9 shows the electron momentum at  $t=10$  for the current profile in Fig. 8. It is clear that the current sheet has broken up into smaller structures, each about an ion Larmor radius long. These smaller structures have a much shorter wavelength than the applied perturbation, thus showing that the short-wavelength instability is more unstable than the long-wavelength one.

Figure 10 shows the electron momentum at  $t=10$ , for a

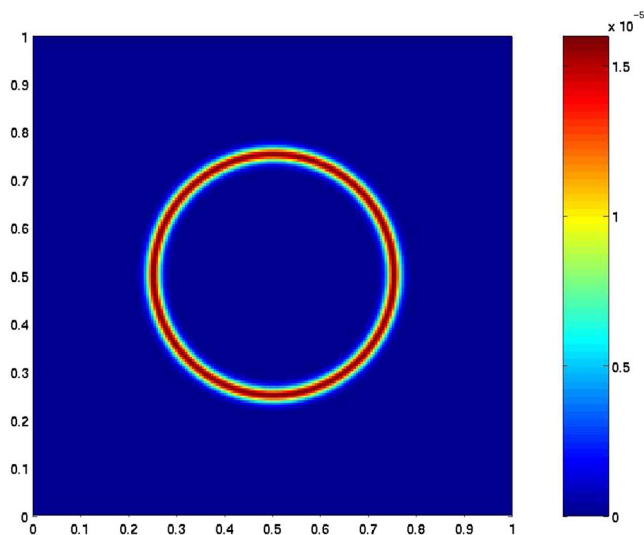


FIG. 8. Electron momentum in the  $r$ - $\theta$  plane for a field reversed pinch. The electrons have an azimuthal velocity, which supports an out-of-plane magnetic field  $B_z$ .

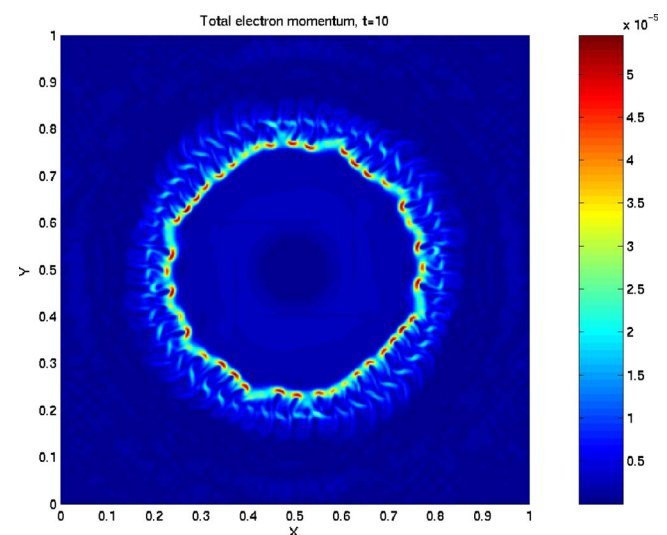


FIG. 10. Electron momentum in the  $r$ - $\theta$  plane for a field reversed pinch at  $t=10$ . The current sheet is thinner than in the previous simulations and is seen to break up into a larger number of pieces.

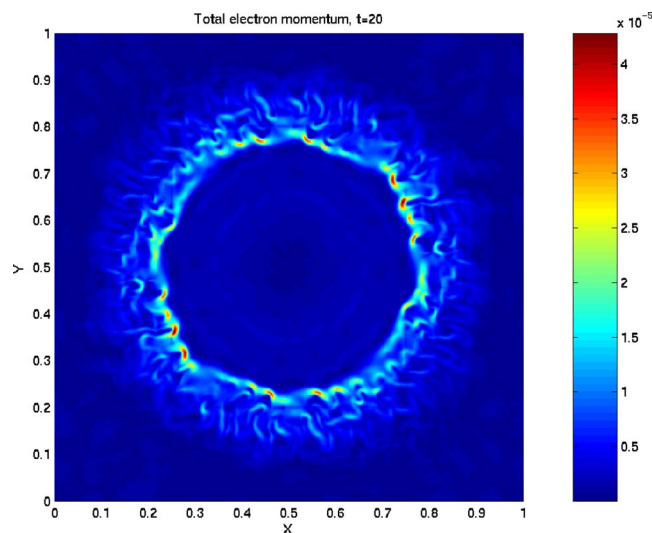


FIG. 11. Electron momentum in the  $r$ - $\theta$  plane for a field-reversed pinch at  $t=20$ . The current sheet has now completely diffused away, and shows many fine-scale features in the electron flow pieces.

thinner current profile than in Fig. 8. With this current profile, the sheet breaks up into finer structures. It is also seen that the sheet has become thicker, which is a typical signature of anomalous resistivity. Figure 11 shows the electron momentum at  $t=20$ . The current sheet has become thicker and the small-scale instability has spread outwards toward the pinch walls.

## VI. LHDI IN PLANAR PLASMA CONFIGURATIONS

To understand the mechanism of the LHDI better, simulations were also performed in planar current sheet geometry. Nonlocal linear theory of this instability has been performed by Yoon, Lui, and Sitnov<sup>27</sup> within the two-fluid model presented here. A Harris current sheet equilibrium was selected. The electron and ion number densities were set to  $n_e = n_i = n(x)$ , where

$$n(x) = n_0 \operatorname{sech}^2(y/L), \quad (47)$$

where  $L$  is the half-width of the current sheet. The magnetic field was initialized by

$$\mathbf{B}(y) = \hat{\mathbf{z}} B_0 \tanh(y/L), \quad (48)$$

where  $\hat{\mathbf{z}}$  is a unit vector in the  $Z$  direction. The electron and ion velocities were set to  $\mathbf{v}_i = \hat{\mathbf{x}} v_i$  and  $\mathbf{v}_e = \hat{\mathbf{x}} v_e$ , where  $v_i$  and  $v_e$  are constants and  $\hat{\mathbf{x}}$  is the unit vector in the  $X$  direction. The initial equilibrium values were perturbed using a perturbation with wavelength given by the domain length.

The current sheet is neutrally stable to the long-wavelength perturbation applied. As the simulation progresses, the sheet simply oscillates about its equilibrium position and appears to “slosh” inside the domain. Figure 12 shows the electron momentum at  $t=100$  and 200. The initial perturbation has kinked the sheet, though the kink does not grow. Figure 12 also shows the electron density at  $t=200$ . It is now seen that small structures are forming at the edge of the current sheet. These structures are each about one ion Larmor radius wide. These structures are a typical signature

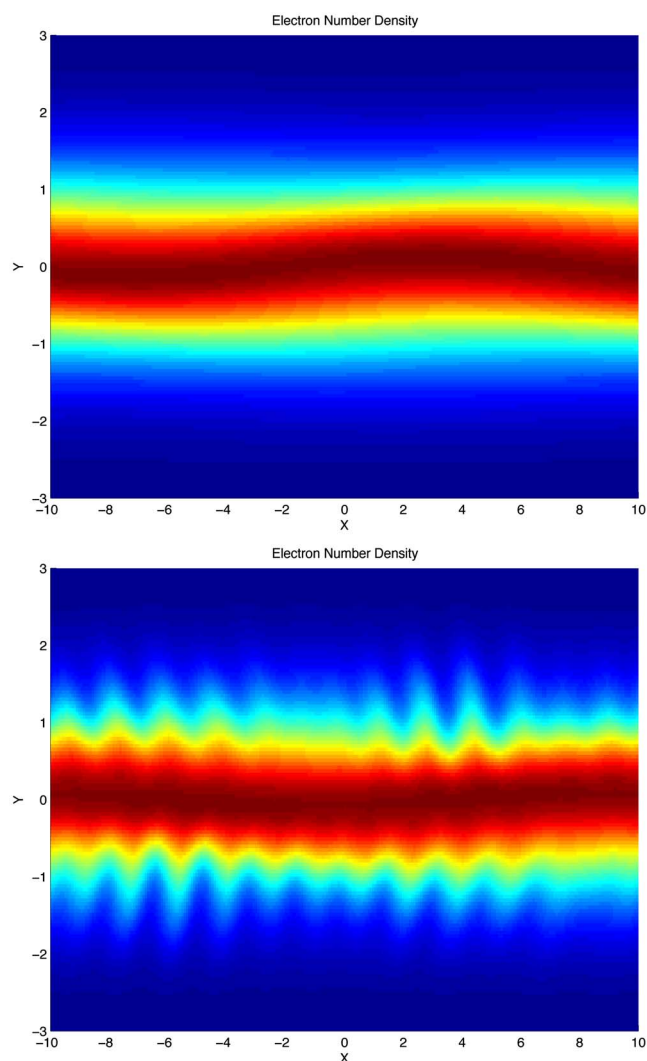


FIG. 12. Electron density at  $t=100$  (top) and  $t=200$  (bottom) for a Harris current sheet kink mode. The sheet is neutrally stable to the applied initial long-wavelength perturbation and simply oscillates about its initial position. At  $t=200$ , lower-hybrid drift instability has just started to form at the edge of the current sheet and is visible as small bumps about an ion Larmor radius thick. The instability grows rapidly after this point soon breaking up the sheet completely.

of the onset of the LHDI, which starts at the location where the density gradient is maximum. Figure 13 shows the electric fields at the same time ( $t=200$ ). The structure of the electric fields in this figure is typically seen in hybrid simulations and typically indicates the onset of the LHDI.

After  $t=200$ , the LHDI instability grows very rapidly, and the “finger”-like structures elongated ultimately breaking up the sheet. Figure 14 shows the electron density at  $t=250$  just as the sheet is about to break up. Two separate perturbations are clearly seen in this figure. The long-wavelength applied kink-mode perturbation is still clearly visible while the short-wavelength LHDI has now almost saturated the flow. This figure dramatically illustrates that although the sheet is stable to the long-wavelength perturbations, it is unstable to the shorter-wavelength LHDI.

Anomalous resistivity was computed from the simulation data as  $\eta = \langle \mathbf{E} \cdot \mathbf{j} \rangle / \langle \mathbf{j} \cdot \mathbf{j} \rangle$ . This was compared to the Spitzer

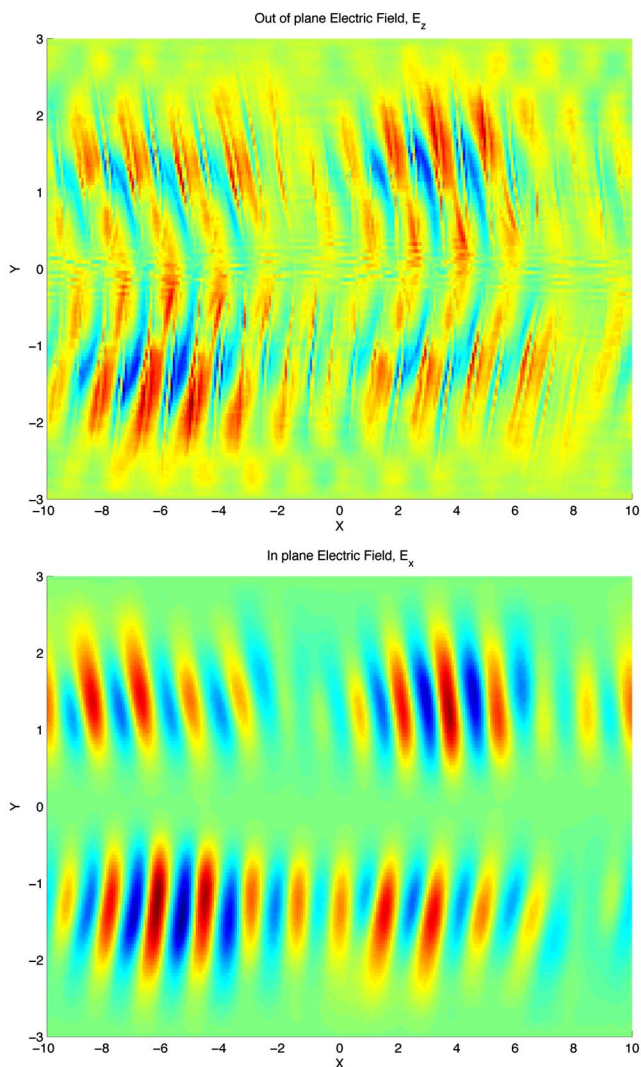


FIG. 13. Out-of plane electric field  $E_z$  (upper panel) and in-plane electric field  $E_x$  at  $t=200$ . The structure of the electric fields seen is a signature of the LHDI in the sheet.

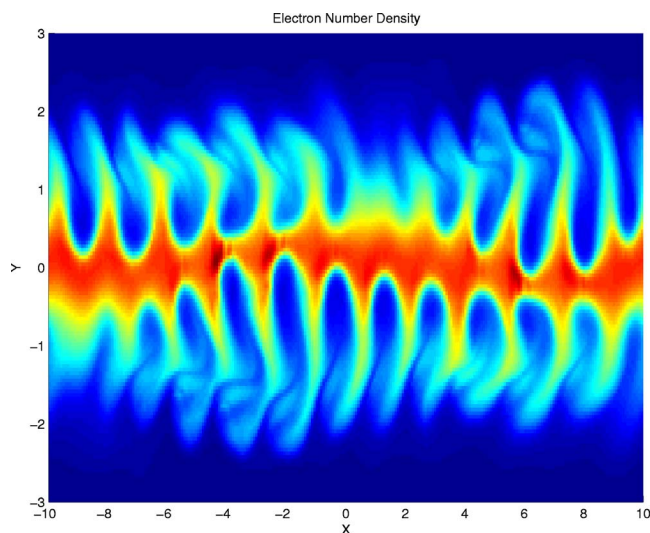


FIG. 14. Electron density at  $t=250$  for a Harris current sheet kink mode. The lower-hybrid drift has now completely set in and the sheet has broken up into thin structures. A secondary Kelvin-Helmholtz instability is also visible as there is a significant velocity shear at the edge of the instability.

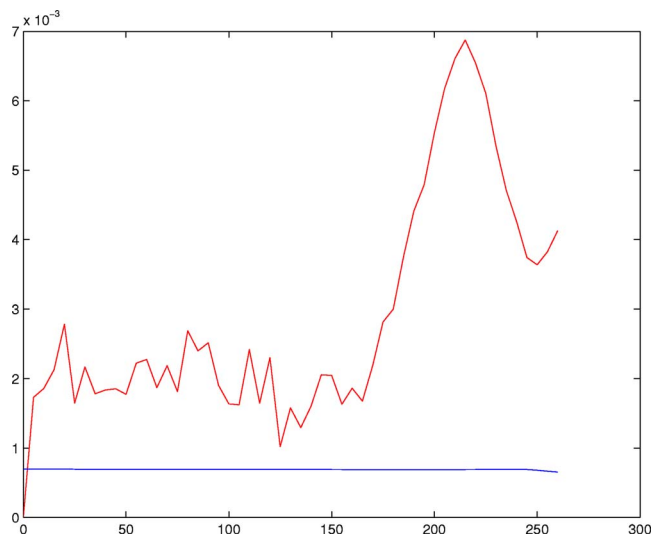


FIG. 15. Average anomalous resistivity (red) estimate as a function of time. The temperature of the fluids does not change in this simulation and thus classical Spitzer resistivity (blue) cannot account for the LHDI.

resistivity value for the simulation parameters. As the temperature of the fluids does not change in the course of the simulation, the Spitzer resistivity remains a constant. From Fig. 15, it is clear that the anomalous resistivity is much higher than the one predicted by Spitzer values. At peak, the anomalous resistivity is about an order of magnitude larger. After the sheet breaks up, the resistivity rapidly decays. This may not be physically accurate, and addition of collisions to the model may help remedy this.

The numerically computed anomalous resistivity was compared to the experimentally measured values from the Translation Sustainment and Confinement (TCS) experiment at the University of Washington. The values are summarized in Table I. The measured and computed values are of the same order of magnitude and hence show that the LHDI is a plausible mechanism for the anomalous resistivity observed in the experiments. These simulations also indicate that FRC lifetime in experiments can be increased if the plasma is kept hotter, or is not allowed to cool rapidly. One way to achieve this would be to minimize the energy loss from radiation due to impurities, a significant loss mechanism in existing experiments.

TABLE I. The average cross-field resistivity determined from absorbed RMF power computed by assuming rigid rotor rotation. Data were obtained from the TCS experiment at the University of Washington.

Shot No.	RMF Field (G)	RMF Freq. (KHz)	$v_d/c_i$	$\eta/\eta_{\text{classical}}$
8966	45.4	114	2.22	11.12
8971	45.4	114	2.34	12.77
8997	38.4	114	2.32	7.97
9071	37.8	114	2.62	12.46

## ACKNOWLEDGMENTS

The authors acknowledge extensive discussions with John Loverich from Advatec Pacific Corporation. We are grateful to the University of Washington's Redmond Plasma Physics Laboratory for providing experimental data. Computer simulations were performed on the Ladon Supercomputer belonging to the Mechanical Engineering Department of the University of Washington. Discussions with Peter Stoltz and Scott Kruger from Tech-X Corporation are acknowledged.

- <sup>1</sup>J. P. Friedberg, *Ideal Magnetohydrodynamics* (Plenum Press, New York, 1987).
- <sup>2</sup>R. J. LeVeque, *Finite Volume Methods for Hyperbolic Problems* (Cambridge University Press, Cambridge, UK, 2002).
- <sup>3</sup>J. Rossmannith, Ph.D. thesis, University of Washington (2002).
- <sup>4</sup>A. Ishimaru, *Electromagnetic Wave Propagation, Radiation and Scattering* (Prentice Hall, Englewood Cliffs, NJ, 1991).
- <sup>5</sup>L. Steinhauer and A. Ishida, *Phys. Plasmas* **5**, 2609 (1998).
- <sup>6</sup>*Space Plasma Simulations*, edited by J. Büchner, C. Dunn, and M. Scholer (Springer, Berlin, 2003).
- <sup>7</sup>*Mathematical Aspects of Numerical Solutions of Hyperbolic Systems*, edited by A. G. Kulikovskii, N. V. Pogorelov, and A. Y. Semenov (Chapman and Hall/CRC, London, 2001).

- <sup>8</sup>D. Bale, R. J. LeVeque, S. Mitran, and J. A. Rossmannith, *SIAM J. Sci. Comput. (USA)* **24**, 955 (2002).
- <sup>9</sup>J. O. Langseth and R. LeVeque, *J. Comput. Phys.* **165**, 126 (2000).
- <sup>10</sup>P. Roe, *J. Comput. Phys.* **43**, 357 (1981).
- <sup>11</sup>*Magnetic Reconnection*, edited by E. Priest and T. Forbes (Cambridge University Press, Cambridge, UK, 2000).
- <sup>12</sup>J. Birn *et al.*, *J. Geophys. Res.* **106**, 3715 (2001).
- <sup>13</sup>M. Hesse, J. Birn, and M. Kuznetsova, *J. Geophys. Res.* **106**, 3721 (2001).
- <sup>14</sup>J. Birn and M. Hesse, *J. Geophys. Res.* **106**, 3737 (2001).
- <sup>15</sup>A. Otto, *J. Geophys. Res.* **106**, 3751 (2001).
- <sup>16</sup>M. Shay, J. Drake, B. Rogers, and R. Denton, *J. Geophys. Res.* **106**, 3759 (2001).
- <sup>17</sup>Z. Ma and A. Bhattacharjee, *J. Geophys. Res.* **106**, 3773 (2001).
- <sup>18</sup>P. Prichette, *J. Geophys. Res.* **106**, 3783 (2001).
- <sup>19</sup>M. M. Kuznetsova, M. Hesse, and D. Winske, *J. Geophys. Res.* **106**, 3799 (2001).
- <sup>20</sup>P. M. Bellan, *Spheromaks* (Imperial College Press, London, 2000).
- <sup>21</sup>A. Ishida, H. Momota, and L. Steinhauer, *Phys. Fluids* **31**, 3024 (1988).
- <sup>22</sup>L. C. Steinhauer, *Phys. Plasmas* **6**, 2734 (1999).
- <sup>23</sup>L. C. Steinhauer, H. Yamada, and A. Ishida, *Phys. Plasmas* **8**, 4053(2001).
- <sup>24</sup>H. Yamada and T. Katano, *Phys. Plasmas* **10**, 1168 (2003).
- <sup>25</sup>H. Yamada, T. Katano, K. Kanai, A. Ishida, and L. C. Steinhauer, *Phys. Plasmas* **9**, 4605(2002).
- <sup>26</sup>E. V. Belova, R. C. Davidson, H. Ji, and M. Yamada, *Phys. Plasmas* **10**, 2361 (2003).
- <sup>27</sup>P. H. Yoon, A. T. Lui, and M. I. Sitnov, *Phys. Plasmas* **9**, 1526 (2002).